WILEY-VCH

Edge-Orientation Dependent Nano-Imaging of Mid-Infrared Waveguide Modes in High-Index PtSe$_2$

Kin Ping Wong, Xin Hu, Tsz Wing Lo, Xuyun Guo, Kin Hung Fung, Ye Zhu, and Shu Ping Lau*

K. P. Wong, Dr. T. W. Lo, Dr. X. Guo, Dr. K.H. Fung, Dr. Y. Zhu, Prof. S. P. Lau
Department of Applied Physics, The Hong Kong Polytechnic University, Hong Kong S.A.R., P. R. China
E-mail: apsplau@polyu.edu.hk

Dr. X. Hu
Institute of Advanced Magnetic Materials, Hangzhou Dianzi University, Hangzhou, 310012, R. China
Key Laboratory of Nanodevices and Applications, Suzhou Institute of Nano-Tech and Nano-Bionics, Chinese Academy of Sciences, Suzhou, 215123, P. R. China

All-dielectric nanophotonics is a rapidly developing field that employs high-index low-loss dielectric materials to boost light-matter interactions at the nanoscale. Owing to their potential in achieving low-loss optical responses and the coexistence of strong enhancement of electric and magnetic fields, which are absent in their plasmonic counterparts. Transition-metal dichalcogenides (TMDCs) have been utilized for high-index dielectric Mie nanoresonators in the visible to near-infrared spectral range due to their high in-plane and out-of-plane optical anisotropy, excitonic effect, and high-index properties. However, high-index materials for mid-infrared (MIR) nanophotonics are still highly sought after. Here, we show that PtSe$_2$, a group 10 TMDC, could support dielectric waveguide modes in MIR despite its semimetallic nature. We reveal that PtSe$_2$ optically acts as a dielectric material with a high refractive index of ~ 5 with a low extinction coefficient in the MIR region. The value is among the highest in the low-loss TMDCs and mainstream dielectric materials. A comprehensive sample-edge-orientation dependent nano-imaging together with spectroscopic nano-imaging characterization of the PtSe$_2$ allows the extraction of the dispersion relations of the modes, from which the velocity parameters could be determined. Our works pave the way for high-performance MIR devices via high-index PtSe$_2$-based nanostructures.

1. Introduction

High-index materials have emerged as a crucial element in nano-optoelectronics and nanophotonics. Promising optical waveguide devices rely on high-index dielectrics to form the core layer for realizing effective optical confinement. Besides, resonant nanostructures made up of high-index dielectrics have received much research interest in recent years for complementing or even replacing plasmonic nanostructures to manipulate light at the subwavelength scale. In contrast to their plasmonic counterparts, which suffer from high metallic dissipative losses, weak magnetic response, and complementary metal oxide semiconductor (CMOS) incompatibility, the high-index dielectric nanostructures supporting resonant optical modes can achieve low-loss optical responses and the coexistence of strong enhancement of electric and magnetic fields, and can be integrated with CMOS platforms.[1] By appropriately constructing the high-index dielectric nanostructures with different geometries and materials, optical responses such as light transmission, absorption, scattering and reflection can be managed effectively, which endows high-index nanostructures with the power to optimize the performance of optoelectronic devices such as photodetectors,[2] optical sources,[3] photoelectrochemical devices[4], photovoltaic cells[5] and nonlinear devices.[6] Moreover, high-index resonant dielectric nanostructures open up opportunities for developing all-dielectric metasurfaces and metamaterials for novel photonic applications such as unidirectional scattering, perfect reflectors, magnetic mirrors, arbitrary light modulation, reflectionless sheets and so on.[7]

TMDCs have been studied intensively due to their exotic electronic and photonic properties.[8] However, researchers did not pay much attention to their high-index properties[9] and also mainly focused on their mono- or few-layer forms. Recently, multilayer TMDCs have been employed to fabricate high-index nanoresonators which support well-defined Mie resonances and anapole states.[10] The high in-plane and out-of-plane optical anisotropy and the excitonic effects of TMDCs were found to have a strong influence on the optical responses of the

nanostructures.[10] Also, ultra-compact waveguides for developing nano-photonic circuits have been fabricated based on these high-index characteristics multilayer TMDCs.[11] While these studies were performed on the group-6 TMDCs (with chemical form MX_2, where M = Mo or W and X = S, Se or Te), less attention has been paid to the emerging Pt-based TMDCs (M = Pt). They were discovered to possess electronic properties highly distinct from their group-6 counterparts, thanks to the strong hybridization between the valance d-orbitals of Pt atoms and the valance p-orbitals of the chalcogen atoms.[12] PtSe2 and PtTe2 were shown to behave as topological type-II Dirac semimetals due to the distinct electronic properties.[13] Recently, near-field characterization was performed on PtTe2 nanoribbons by the scattering-type scanning near-field optical microscopy (s-SNOM), which enables nanoscale optical imaging with wavelength-independent spatial resolution. It thus has been widely employed for research in near-field optics of van der Waals (vdW) layered materials.[14] It was shown that the semimetallic PtTe2 supports layer-dependent surface plasmon polaritons (SPPs) in the MIR region.[15] PtSe2 has been perceived as one of the most promising materials for future nano-electronics and nanophotonics due to its exceptional properties, especially the long-term air stability, high charge-carrier mobility, and unique thickness-dependent semiconductor to semimetal phase transition.[16] However, its near-field characterization has yet to be performed on it. In this work, we performed near-field imaging on PtSe2 flakes at the MIR window by employing the s-SNOM. Interestingly, the obtained near-field images were sensitive to the orientation of the sample-edge relative to the incident direction of the illuminating beam, which is a characteristic of dielectric waveguide modes, rather than the metallic SPPs.[17] To confirm the unexpected dielectric-waveguide-supporting properties of the semimetallic PtSe2 flakes, both far-field and near-field Fourier transform infrared spectroscopies (FTIRs) (that is, the conventional FTIR and the nano-FTIR) were performed. We found that PtSe2 optically acts as a dielectric material with a high refractive index of ~ 5 with low extinction coefficient in the MIR range. This effect should be attributed to PtSe2

having a much lower plasma frequency than PtTe2. The refractive index of PtSe2 was found to be much larger than most of the other low-loss TMDCs (~ 3 – 4)[9] and typical MIR dielectric materials such as Si (~ 3.43)[18] and Ge (~ 4.02).[18] After confirming the PtSe2 flakes support high-index dielectric waveguide modes, we studied the aforementioned sample-edge orientation dependence property in detail, by investigating the influence on the s-SNOM images when rotating the sample with respect to the incident direction of the excitation beam. This, together with spectroscopic nano-imaging, allows the extraction of dispersion relations of the modes, from which the phase and group velocities and the group velocity dispersion (GVD) of the modes were determined.

2. Results and Discussion

2.1. TEM Characterization of PtSe2 Planar Waveguides

The PtSe2 planar waveguides studied here were fabricated by gel-assisted mechanical exfoliation[19] of a bulk PtSe2 crystal onto standard SiO2/Si wafers (see Experimental Methods for the sample fabrication). **Figure 1**a shows the crystal structure of the PtSe2 along the [210] and [001] directions. The theoretical lattice spacings for the (001) and ($1\bar{2}0$) planes are labelled, based on the calculated lattice constants $a = b = 3.785$ Å and $c = 4.969$ Å.[13a] Being a 1T-phase material, PtSe2 crystallizes in the layered CdI2-type structure with $P\bar{3}m1$ space group and D_{3d}^3 point group, that is, the octahedral structure, in which each Pt atom is enclosed by six Se atoms to form a PtSe6 octahedron and each PtSe2 layer is formed by these edge-sharing octahedra. The three-dimensional structure is formed by stacking the PtSe2 layers. In each layer, the Pt 2D-layer is sandwiched between the two Se 2D-layers.

Figure 1b,c shows the cross-sectional high-angle annular-dark-field scanning transmission electron microscopy (HAADF STEM) Z-contrast image with the electron beam along [210] direction and the corresponding energy dispersive X-ray spectroscopy (EDS) maps of a 660-nm-thick PtSe2 planar waveguide. The EDS maps reveal the uniform distribution of the Pt and

Se elements, indicating the pure chemical composition of the $PtSe_2$. In addition, Figure 1d,e

shows the low-resolution TEM and high-resolution TEM (HRTEM) images, respectively,

again with the electron beam along the [210] direction. The latter indicates lattice fringes with

spacing 5.0 Å and 1.9 Å for the (001) and ($1\bar{2}0$) planes respectively, which is consistent with

the theoretical values as shown in Figure 1a. Furthermore, the corresponding selected area

electron diffraction (SAED) pattern (Figure 1f) reveals the single-crystallinity of the $PtSe_2$.

All these analyses confirm the high crystal quality of the $PtSe_2$ planar waveguides for the

optical study.
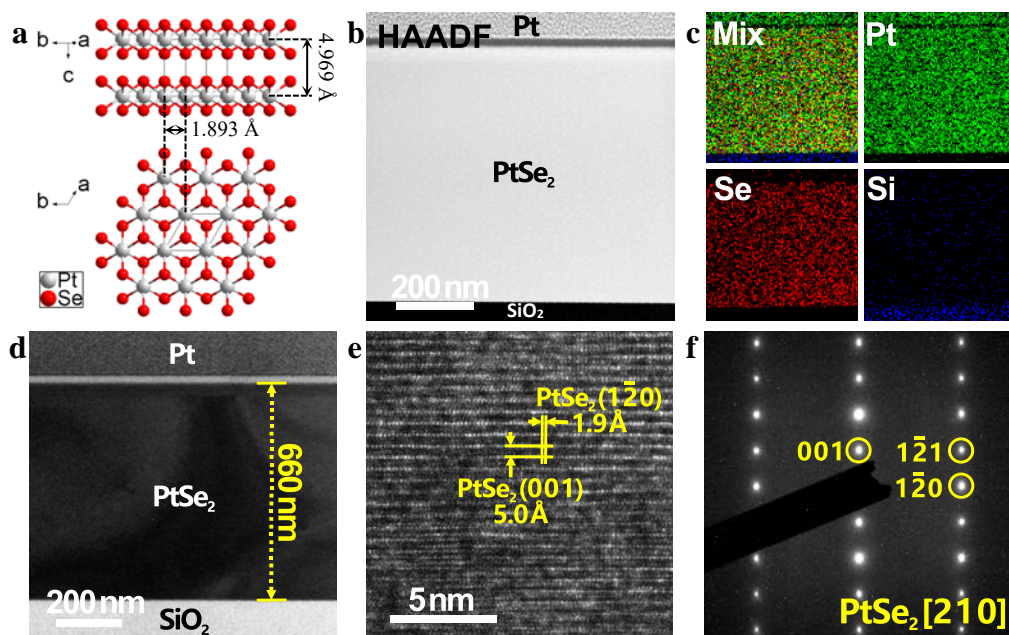
Figure 1. Crystal structure of $PtSe_2$ and TEM characterization of a $PtSe_2$ planar waveguide. (**a**) Crystal structure model of the $PtSe_2$ along the [210] (top image) and [001] (bottom image) directions. The unit cells are indicated by black lines. (**b**) Cross-sectional HAADF STEM Z-contrast image with the electron beam along the [210] direction. (**c**) The corresponding EDS elemental mapping of (b). (**d**, **e**) Cross-sectional low-resolution and high-resolution TEM images, respectively, with electron beam along the [210] direction. (**f**) The corresponding SAED pattern of (e).

2.2. Nano-imaging of PtSe$_2$ Waveguides

Figure 2a,b illustrates the 3-dimensional view and top view of the experimental set-up, respectively. The tip scanning was performed in the region near a specific sample edge (the investigated edge) and away from the others, as indicated by the light blue dashed-line rectangle. The coordinate system is defined such that the origin point O lies at the investigated edge, with reference to which the x-direction represents the alignment of the edge. The y-direction represents the edge orientation, and the z-axis refers to the distance above the sample surface. During the scanning, a p-polarized (namely the electric field along the plane of incidence) MIR laser beam with free-space wavenumber k_0 (= $200\pi\omega$, where ω is the spectroscopic wavenumber with unit cm^{-1}) and incident angle $\alpha = 40°$ with respect to the sample surface (x-y plane) is focused onto the apex of the metalized tip. Thus, the polarized beam generates a strong near-field at the apex with a size comparable to the apex radius of curvature $a \approx 30$ nm. Such a near-field hotspot interacts with the sample underneath the tip, thereby generating a near-field back-scattered signal (see Experimental Methods for the s-SNOM set-up). Also, the near-field hotspot can provide sufficient momentum to overcome the momentum mismatch between the waveguide modes and free-space photons.[20] Thereby, the waveguide modes propagate inside the PtSe$_2$ sample and generate cylindrical evanescent waves near the sample surface, which is represented by the ripples as shown in Figure 2. As shown in Figure 2b, an angle β is introduced to specify the investigated edge orientation (y-direction). This sample-edge-orientation angle β is defined as the angle between the x-axis and the projected incident wavevector $\mathbf{k}_{inc,\|}$.
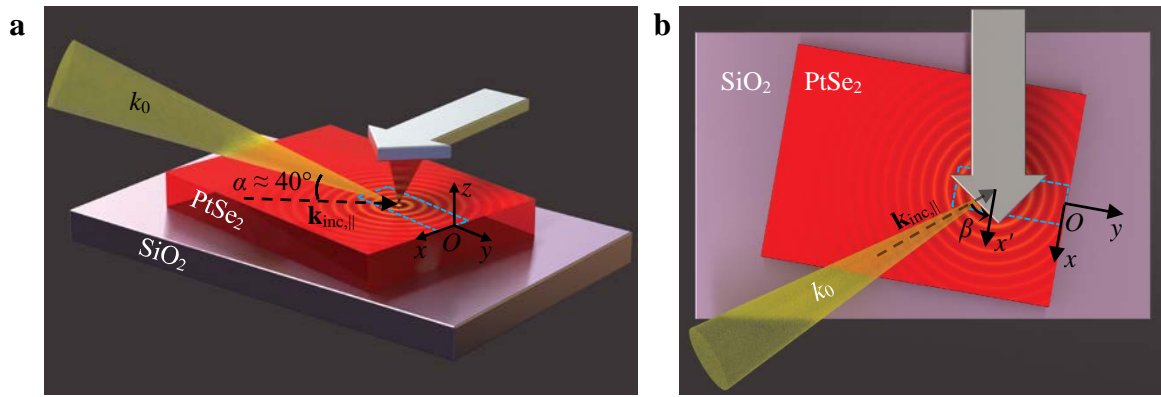
**Figure 2.** Schematic diagrams of near-field imaging on a PtSe$_2$ sample by the use of the s-SNOM. (**a**) 3-dimensional and (**b**) top view schematic diagrams. A p-polarized MIR laser beam with free-space wavenumber k_0 and with incident angle $\alpha \approx 40°$ is focused onto the AFM probe tip to create a strong near-field near the tip apex, which in turn launches the waveguide modes propagating radially inside the PtSe$_2$ layer. The corresponding evanescent wave on the sample surface is indicated by the ripples in (a) and (b). The nano-imaging is performed by scanning the region near a specific sample edge and away from the others, which is indicated by the light-blue dashed rectangle. The coordinate system is defined such that the specific edge is aligned to the x-axis and is orientated to the y-direction. Accordingly, the sample-edge-orientation angle β is defined as the angle between the projected incident wavevector $\mathbf{k}_{inc,\parallel}$ and the x-axis, as illustrated in (b).

Figure 3a shows the s-SNOM s_3 image and the corresponding lateral line-profile (blue line) of a 579-nm-thick PtSe$_2$ sample (see Figure S1a in the Supporting Information for the AFM topography) with excitation frequency $\omega = 2519$ cm^{-1} and at $\beta = 60°$. The s_3 signal is obtained by demodulating the near-field scattered light at the 3rd order harmonic of the oscillation frequency of the AFM tip to filter out the background signal (see Experimental Methods for the detail of signal filtering). From the top view (inset of Figure 3a), the orientation (y-direction) is toward the right, and the alignment of the investigated edge (x-direction) is parallel to the AFM cantilever. Figure 3b shows the s-SNOM image and the corresponding line-profile for the same scanning region (marked by the light blue dashed-line rectangles in the insets of Figure 3a,b) after rotating the PtSe$_2$ flake by 180° counterclockwise such that $\beta = 240°$. In this case, the investigated edge orients to the left and still aligns parallel to the cantilever. From the images (and line-profiles) in both cases, the interference fringes parallel to the investigated edge (marked by the green dashed-lines) are observed. In each image, the

fringe pattern is a superposition of oscillations with different periodicities (ρ). Despite the same scanning region and similar configurations in both cases, the fringe patterns are different because of their dependence on the edge orientation. One of the differences is that the base-signal appears to be a modulation with a minimal spatial frequency for $\beta = 240°$ but appears to be a constant for $\beta = 60°$ (cyan dash-lines in Figure 3a,b). Figure 3c,d shows the s-SNOM images (and corresponding line-profiles) after subtracting the base-signals. While the base-signal-subtracted image for $\beta = 60°$ remains similar to the original one, the image for $\beta = 240°$ recovers the decay appearance like the one for $\beta = 60°$. By comparing the base-signal-subtracted images, one can see that for $\beta = 240°$ the interference pattern has larger fringe spacing generally. By quantitatively comparing the compositions of the fringe patterns, we perform Discrete Fourier Transform (DFT) on the base-signal-subtracted line-profiles and the resulting q-space profiles (shown in Figure 3e,f). The peaks directly refer to the inverse fringe-periods ($q_\rho = 2\pi/\rho$) of the air mode or waveguide modes of different types identified by the dispersion analysis below and marked by the colored inverted triangles. Consistent with the above observation that generally the fringe spacing is larger for $\beta = 240°$ than $\beta = 60°$, the waveguide modes with the same types have smaller q_ρ for $\beta = 240°$ than $\beta = 60°$, although each waveguide mode (wm) of certain type should have a specific propagation constant q_{wm}.
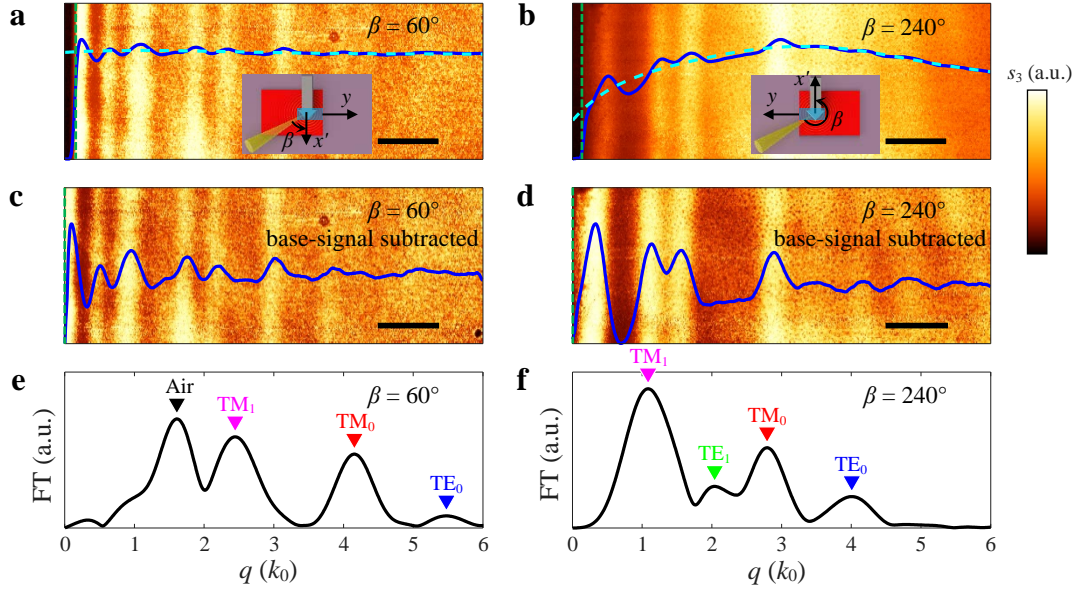
Figure 3. Results for the near-field imaging on a 579-nm-thick PtSe$_2$ planar waveguide with excitation frequency 2519 cm^{-1} for configurations $\beta = 60°$ and $\beta = 240°$. (**a**) The s-SNOM image for $\beta = 60°$. The scanning area, which is 15 μm × 5 μm, is indicated by the highlighted blue areas in the inset. (**b**) The s-SNOM images generated by rotating the sample in (a) 180° anticlockwise such that $\beta = 240°$ and then scanning the same area (inset). The corresponding line-profiles and the base-signal profiles of the images in (a) and (b) are represented by the blue lines and cyan lines, respectively. Both images consist of interference fringe patterns parallel to the edge (green dash-lines) induced by the waveguide modes supported by the PtSe$_2$ and are shown to be β-dependent. (**c, d**) Base-signal-subtracted images of (a) and (b) respectively. Scale-bars in (a-d) represent 2 μm. (**e, f**) Momentum-space profiles were obtained by performing DFT on the base-signal subtracted line-profiles in (c) and (d), respectively. The peaks directly refer to the inverse fringe-periods q_ρ of different modes, whose types are identified by the dispersion analysis below and marked by the colored inverted triangles.

The sample-edge-orientation dependence of the fringe patterns suggests that the modes supported by the system are neither SPPs (supported by metallic materials such as graphene) nor surface-phonon-polaritons (SPhPs) (supported by polar materials such as h-BN). In contrast, Hu *et al.* have found that dielectric waveguide modes can induce interference fringes that are sensitive to the sample-edge-orientation and are in good agreement with our results.[17b] Figure S2 illustrates their proposed signal collection mechanism for $\beta = 60°$ and $\beta = 240°$ configurations. When the probe tip is illuminated by the incident beam (with wavevector $\mathbf{k}_{inc}$), it induces two parts of signals. The first part is the tip-scattered free-space light, which is common for any s-SNOM study. Due to the small collection angle, the

parabolic mirror only efficiently collects the portion of tip-scattered light with wavevector ($\mathbf{k}_{sca,tip}$) parallel to the incident beam ($\mathbf{k}_{inc}$). The blue arrow in each subfigure represents the pathway of this light. For the second part, each tip-launched waveguide mode (ripples in Figure 2, with propagation vector $\mathbf{q}_{wm}$) could propagate to the investigated edge, and in turn, scatters to free-space light in air with wavevector $\mathbf{k}_{sca,edge}$ parallel to $\mathbf{k}_{inc}$ (and $\mathbf{k}_{sca,tip}$), and is collected efficiently by the parabolic mirror. The addition of the two green arrows represents this second pathway. As illustrated in the top views in Figure S2a,b, for each waveguide mode, it is the portion that travels with an angle ϕ from the y-direction, which efficiently generates the edge-scattered light parallel to the incident light, due to the conservation of the momentum along the edge direction. By this signal collection scheme, it is the interference between the tip-scattered light and the edge-scattered light which generates the fringe patterns in the s-SNOM images (Figure 3). As shown in Figure S2, for different edge-orientations, although the optical path length (OPL) for the first pathway is the same, it is different for the second pathway, resulting in edge-orientation dependence of the fringe pattern. Quantitatively, the inverse fringe-period q_ρ in the s-SNOM images and the propagation constant q_{wm} are related by

$$q_\rho = q_{wm} \cos\phi + k_0 \sin\beta \cos\alpha \tag{1}$$

with $\phi = \sin^{-1}\left(\left(\frac{k_0}{q_{wm}}\right)\cos\alpha\cos\beta\right)$ (see Supporting Information Section S1 for the derivation). The equation obviously reveals that, for a waveguide mode with a specific propagation constant q_{wm}, the corresponding inverse fringe-period q_ρ of the mode varies with the sample-edge-orientation angle β. There may be other mechanisms that can also induce fringe patterns in s-SNOM images. Their impact on the s-SNOM images in this work are discussed in Section S3.

2.3. Far-field FTIR Spectroscopy

To confirm the MIR-waveguide properties of PtSe2, far-field Fourier-transform infrared

spectroscopy (FTIR) study was carried out. The resulting reflectance spectrum R(ω) with

frequencies ranging from 1000 to 3000 cm^{-1} for a 1708-nm-thick PtSe2 on an Au substrate is

shown by the black line in **Figure 4**a. The reflectance spectra in the full MIR range as a

function of PtSe2 thickness are shown in Figure S3. From the spectrum, we observe the

Fabry–Pérot (FP) interference, which is a characteristic of waveguides. As the optical

constant of a metallic material can be expressed by the Drude-Lorentz (DL) model,[21] we

assume that the in-plane complex dielectric constant of PtSe2 can be written with a single

Lorentzian oscillator term as

$$\varepsilon_{\parallel}(\omega) = \varepsilon_{\infty} - \frac{\omega_p^2}{\omega^2 + i\gamma_D\omega} + \frac{f^2}{\omega_0^2 - \omega^2 - i\gamma_L\omega},$$ (2)

where ε_{∞} is the high-frequency dielectric constant, ω_p and γ_D are the plasma frequency and

collision frequency of free charge carriers respectively, and f, ω_0 and γ_L are the strength,

eigenfrequency and damping rate of the Lorentzian oscillator respectively. The second term is

the Drude term which refers to intraband transition of the free charge carriers while the third

term is associated with the effect of interband transitions of the bound charge carriers.

Previous studies have found that the concentration and the effective mass of the free charge

carriers of bulk PtSe2 are $N = 1.7 \times 10^{20}$ cm^{-3} [22] and $m^* = 2.5m_e$,[23] respectively, where m_e is

the electron rest mass. Using these values, the plasma frequency ($\omega_p = \sqrt{\frac{Ne^2}{\varepsilon_0 m^*}}$, where e and ε_0

are the elementary electric charge and vacuum permittivity, respectively) is determined to be

2470 cm^{-1} (0.306 eV). By fitting the reflectance spectrum (red dashed line in Figure 4a),[24]

the other parameters are determined to be $\varepsilon_{\infty} = 1$, $\gamma_D = 277$ cm^{-1}, $f = 81872$ cm^{-1}, $\omega_0 = 15683$

cm^{-1} (1.94 eV) and $\gamma_L = 2822$ cm^{-1} (see Experimental Methods and also Section S4 for the

fitting methodology). Kramers-Kronig (KK) analyses are then performed on the DFT

spectrum in a frequency range extended to the NIR region (Figure S4), and the resulting phase

spectra $\theta(\omega)$ are plotted in Figure 4b (see Experimental Methods and also Section S5 for the methodology). The qualitative agreement between the result and the theoretical phase spectrum calculated using the fitted dielectric constant further validates the reliability of the model. Thus, the complex ordinary refractive index $\tilde{n}_o = n_o + i\kappa_o$ of the PtSe2 can be calculated (Figure 4c), where the real part n and imaginary part κ represent the refractive index and the extinction coefficient of PtSe2, respectively. PtSe2 possesses a high ordinary refractive index ($n_o \sim 5$), which is greater than SiO2 [25] and Si.[26] This implies that the waveguide modes in the PtSe2 planar waveguide (air/PtSe2/SiO2/Si structure) are mainly confined to the PtSe2 layer. Table 1 compares both the ordinary (n_o) and extraordinary (n_e) refractive index of PtSe2 with the typical high-index MIR dielectric materials (Si and Ge) and some MIR dielectric TMDCs. The extraordinary refractive index of PtSe2 was assumed to be 0.8 times the value of the ordinary one, as will be explained in the dispersion analysis below. From the extracted extinction coefficient, we can obtain the skin depth (δ) of the PtSe2, which is plotted in Figure 4. The high value of skin depth (> 80 μm) further suggests the waveguide-supporting-property of the PtSe2.
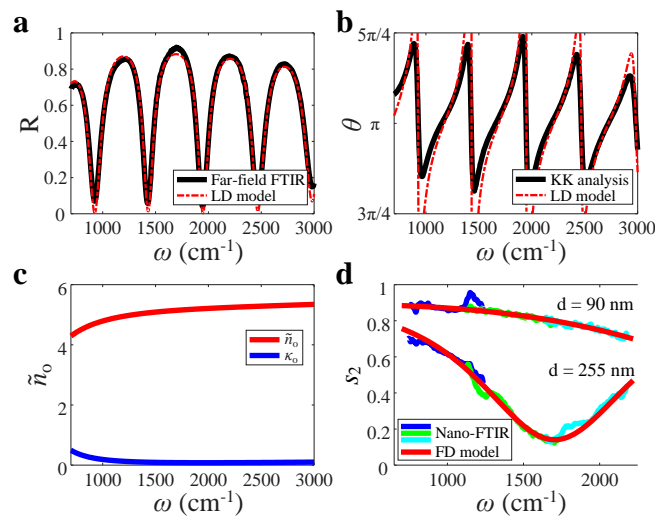
Figure 4. Optical constant extraction of PtSe2 by far-field (conventional) and near-field (nano-) FTIR studies. (**a**) The FTIR (black line) and calculated (red dashed line) reflectance spectra $R(\omega)$ of a 1708 nm thick PtSe2 sample on an Au substrate. The

calculated spectrum is based on the fitted in-plane dielectric constant $\varepsilon_\parallel(\omega)$ of PtSe$_2$ according to the DL model. The observed FP interference effect suggests the waveguide-supporting property of PtSe$_2$. (**b**) The reflection phase spectrum $\theta(\omega)$ generated by performing KK analysis on the FTIR spectrum in (a) (black line) and by calculation based on the fitted $\varepsilon_\parallel(\omega)$ of PtSe$_2$ (red dashed line). (**c**) The complex ordinary refraction index $\tilde{n}_o$ = n_o + iκ_o, calculated based on the fitted $\varepsilon_\parallel(\omega)$. The real part ($n_o$) and imaginary part ($\kappa_o$) represent the ordinary refractive index and the extinction coefficient, respectively. (**d**) The 2nd order demodulated near-field amplitude spectra (normalized to Au) of the 90 nm and 255 nm thick PtSe$_2$ samples on Au substrates. The experimental spectra are composed of different portions (blue, green, and cyan lines), which were generated by performing nano-FTIR with laser sources with different bands. The theoretical spectra (red lines) were calculated based on the fitted $\varepsilon_\parallel(\omega)$ and the extended FD model.

2.4. Near-field FTIR Spectroscopy

Besides conventional far-field FTIR, we also perform nanoscale near-field FTIR (nano-FTIR) to characterize the optical properties of PtSe$_2$ (see Experimental Methods for more detail about nano-FTIR). Figure 4d shows the 2nd order demodulated near-field amplitude spectra $s_2(\omega)$ (normalized to Au) of the 90 nm and 255 nm thick PtSe$_2$ samples on Au substrates. Each experimental spectrum of the two samples is composed of different parts (blue, green and cyan lines), which were generated by nano-FTIR with various (broadband) laser bands. We observe that there is an intensity trough for the 255 nm thick sample near 1700 cm^{-1}, while it does not appear for the 90 nm thick sample. This phenomenon should be attributed to the high-refractive-index and waveguide-supporting property of PtSe$_2$. To explain that, one should refer to the relation[27]

$$s \propto \left(1 + r_p\right)^2 \alpha_{\text{eff}}, \tag{3}$$

where s is the near-field amplitude, α_{eff} is the effective polarizability of the AFM tip, and r_p is the complex-valued Fresnel's reflection coefficient of the Air/PtSe$_2$/Au layered system for p-polarized light. Equation (3) states that the near-field response is directly proportional to α_{eff} and also the factor $(1 + r_p)^2$. The latter proportionality is introduced due to the additional illumination on the tip and additional backscattered light, caused by the reflection of the incident and backscattered light, respectively, at the sample surface. From Figure 4a,b, we observed that the high-refractive-index PtSe$_2$ enables the Air/PtSe$_2$/Au system to support the

WILEY-VCH

FP cavity effect so that the modulus and phase r_p of the system oscillate within the MIR window. For the 255 nm thick PtSe$_2$ sample, this effect made the factor $(1 + r_p)^2$ in Equation (3) oscillate and thus induced a trough in the near-field spectrum. The trough occurs when r_p = -1, which means the z-component (along the tip, Figure 2a) of the incident illuminating field is in antiphase with the reflected illuminating field. For the 90 nm thick PtSe$_2$ sample, there was no minimum because the smaller thickness made the intensity oscillation much slower. In Figure 4d, we also show the theoretical near-field spectra (red lines), which were generated by using the fitted dielectric constant of PtSe$_2$ from far-field FTIR. By employing the extended finite dipole (FD) model[28] to calculate α_{eff} in Equation (3) for the near-field response for such a layered structure (see Experimental Methods and Section S6). From the experimental spectrum of the 255 nm thick PtSe$_2$ sample, we observed that the intensity minimum did not reach a value of zero. However, it was expected from the factor $(1 + r_p)^2$ in Equation (3). This factor is commonly added for the near-field spectrum calculation. Still, previous research of near-field spectroscopy was mainly for relatively thin samples and low-dielectric materials, for which the FP cavity does not affect the spectra pronouncedly. Here we studied the near-field response of a material combined with the FP effect. We hypothesized that the incident illuminating and reflected illuminating fields (also the direct backscattered and reflected backscattered fields) cannot couple completely near the AFM tip, which could be due to the field retardation and the antenna effects of the tip or the influence of the sample underneath the tip. We added a phenomenological factor 0.5 to r_p in Equation (3) to account for the incomplete coupling effect. From Figure 4d, one can see the theoretical and experimental results are consistent with each other.

14

Table 1. Comparison of the ordinary (n_o) and extraordinary (n_e) refractive index of $PtSe_2$ with Si and Ge, the typical MIR dielectric materials, and selected low-loss TMDCs, at the MIR frequency 2000 cm^{-1} (0.25 eV).

Materials	n_o	n_e	References
$PtSe_2$	5.21	4.66	This work
PtS_2	4.07	3.07	[9]
$MoTe_2$	4.24	2.96	[9]
$MoSe_2$	4.21	2.57	[9, 26]
MoS_2	3.87	2.49	[9, 29]
WSe_2	3.70	2.60	[9, 30]
WS_2	3.53	2.37	[9, 30]
$ZrSe_2$	2.74	2.58	[9, 31]
ZrS_2	2.58	2.31	[9, 31]
$HfSe_2$	2.48	2.42	[9, 31]
HfS_2	2.24	2.20	[9, 31]
$SnSe_2$	3.21	2.83	[9, 32]
SnS_2	3.16	2.40	[9, 32]
Si	3.43	3.43	[18]
Ge	4.02	4.02	[18]

2.5. Sample-edge Orientation Dependent Nano-imaging

We have observed in Figure 3 that the tip-induced waveguide modes lead to sample-edge-orientation dependence of the interference patterns in the s-SNOM images. **Figure 5**a shows the base-signal-subtracted images of the 579 nm thick $PtSe_2$ sample and with excitation frequency 2519 cm^{-1} for various sample-orientation angles (β) that cover a full angle cycle. Due to the base-signal-subtraction process, the signal modulation with small-spatial-frequency is removed, which is especially pronounced in the region $\beta > 180°$, as shown in the original images (Figure S6). The interference fringe pattern in each image reveals intensity decaying from the sample edge ($d = 0$ μm), due to the cylindrical nature of the tip-induced waveguide modes. From these images, we observe that the fringe patterns vary systematically

15

with β. Same as above, we performed DFT on the line-profiles (Figure S7a) to analyze these complicated fringe patterns. The resulting DFT profiles are given in Figure S7b. The peaks in each profile represent the inverse-periods (q_ρ) of the fringes generated by the air mode or waveguide modes, whose types are identified by the dispersion study below and are indicated by colored squares. Generally, the q_ρ of each mode are higher in the region $0° < \beta < 180°$ than in the region $180° < \beta < 360°$. This effect could be attributed to the factor $\sin(\beta - \phi)$ in Equation (1). By fitting Equation (1) to the experimental q_ρ data points, we determine the propagation constant q_{wm} (and therefore the momentum) of each mode (Figure 5b). Figure 5b shows that the theoretical prediction is consistent with the experimental results, except for the regions near $\beta = 0°$ and $\beta = 180°$, which may be caused by the measurement artifact associated with the residual non-linear oscillation component of the probe tip.[33] Figure 5b also shows that the air mode is unresolved for $\beta > 180°$. In theory, the air mode has small q_ρ for the second half cycle of β (the back dashed line in Figure 5b), and therefore the fringes induced by the air mode should have very large periodicities. This is consistent with the observation that the original s-SNOM images for $\beta > 180°$ possess signal modulations with small spatial frequencies (Figure S6). As a result, the air mode is not resolved after the base-signal-subtraction. The air mode is the free-space propagation of photons in air above the SiO_2 substrate and is thus independent of the waveguide modes.[11a] Therefore, removing the air-mode-induced signal-modulation does not omit important information, but even favors the analysis of the waveguide modes.
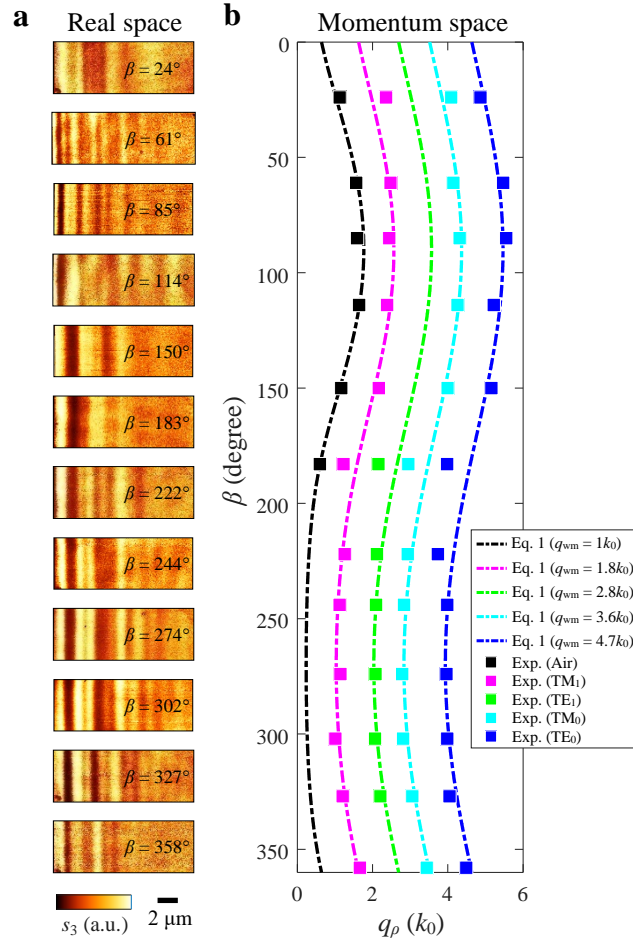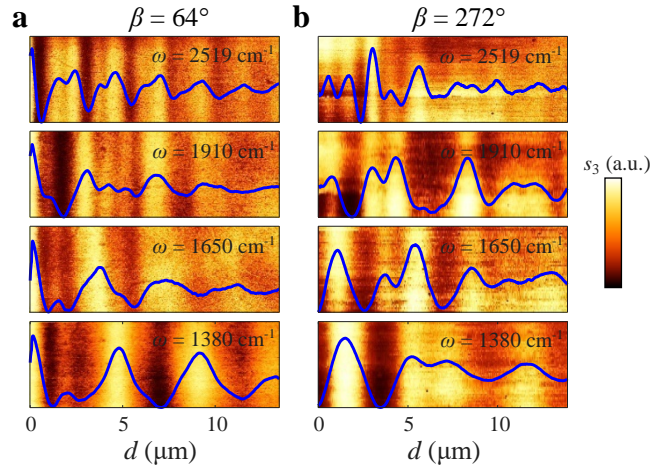
Figure 5. Sample-edge-orientation dependence of the waveguide-mode-induced fringe patterns. (**a**) The base-signal-subtracted s-SNOM images of the 579 nm thick $PtSe_2$ planar waveguide with excitation frequency 2519 cm^{-1} for different orientation angles (β), which altogether cover a full angle cycle. The scanning area is 15 μm × 5 μm. Scale-bar: 2 μm. (**b**) The β-dependence of the inverse fringe-periods q_ρ of different modes, whose types are identified by the dispersion analysis. Experimental data points (colored squares) are extracted by performing DFT on (a) (see Figure S7). Theoretical lines are plotted by choosing suitable q_{wm} values to fit Equation (1) to the experimental points.

It should be noted that in Figure S7b the DFT intensities of transverse electric (TE) modes are generally smaller than transverse magnetic (TM) modes. Moreover, the TE_1 mode cannot be resolved in the first half of the angle cycle. A potential reason is that the common s-SNOM, which is equipped with a p-polarized illuminating beam, favors the excitation of TM modes over TE modes.[34] Although the p-polarized beam has an in-plane component, the elongated probe geometry facilitates the light-probe coupling to generate stronger local field enhancement along the tip axis than along the sample plane.[35] Notwithstanding, the p-

polarized s-SNOM has been successfully employed for generating tip-induced TE polarized

waveguide modes in the VIS and NIR regions[11b, 17a] and which was extended to the MIR

region in this work. The excitation is feasible as the relatively small momenta of the modes

when compared to other EM surface modes such as the SPPs in graphene. The propagation

constants (q_{wm}) of the guided modes in this work are just single-digit multiples of k_0, while for

graphene SPPs they can be over tens of times the value of k_0 and thus the fine tip is necessary

for providing the huge momentum mismatch to excite the SPPs.

Figure 6. Spectroscopic nano-imaging. (**a**) The base-signal-subtracted s-SNOM images of a 696 nm thick PtSe$_2$ planar waveguide with various excitation frequencies for $\beta = 64°$ edge-orientation. (**b**) The images taken in the same area in (a) after rotating the sample such that $\beta = 272°$. The abscissa (d) represents the distance from the edge.

2.6. Dispersion Analysis

Following the study of sample-edge-orientation dependence of the fringe patterns, we explore

their excitation-frequency (ω) dependence. **Figure 6**a,b shows the base-signal-subtracted s-

SNOM images and their corresponding line-profiles of a 696 nm thick PtSe$_2$ sample (see

Figure S1b for the AFM topography) with different excitation-frequencies for $\beta = 64°$ and $\beta =$

272° configurations respectively (see Figure S8 for the original images). From the

spectroscopic images we observe that the fringe periods generally increase, and the fringe

patterns become less complex when ω decreases. This is because the propagation constants

(q_{wm}) of the modes generally decrease with ω and the TE$_1$ mode disappears when ω is below

approximately 1700 cm^{-1}, as shown by the theoretical dispersion relations $\omega(q_{wm})$ of the

waveguide modes in **Figure 7**, which are represented by the bright regions of the pseudo-

color maps or equivalently by the dashed lines. The dispersion color maps are obtained by

calculating the loss function $L = \text{Im}(r_{(s,p)})$, where $r_{(s,p)}$ is the Fresnel's reflection coefficients of

the layered structure for the s- and p-polarized light. L is a quantitative measurement of the

optical losses during light-matter interaction. Therefore, the peaks (bright regions) of L refer

to high loss in energy (i.e. strong absorption) that denotes the excitation of long-life modes.[36]

For the dispersion curves, they are obtained by numerically solving the transcendental

eigenequations of the waveguide modes (Equation (S17) and (S18)). Refer to the

Experimental Methods and Section S7 for the details of the dispersion calculation. From the

dispersion curves, the group velocities of the modes are determined to be about $0.13c - 0.18c$,

where c is the speed of light in vacuum, with nearly zero GVD (Figure S10). In Figure 7, we

also plot the experimental dispersion data points which are superimposed on the theoretical

dispersion relations. They are obtained by performing DFT on the line-profiles in Figure 6 to

determine the corresponding inverse periods (q_ρ) (see Figure S9 for the resulted FT profiles),

followed by conversion to the propagation constants (q_{wm}) by numerically solving Equation

(1). From Figure 7, one can see that the extracted points from the $\beta = 64°$ and $\beta = 272°$ images

are also consistent with one another, which further confirms the validity of Equation (1). The

slight deviation of the extracted points of the TE$_1$ mode from the two β configurations may be

due to the weak excitation and short propagation length (see Section S8 and Figure S11),

compared to other modes. Notwithstanding, the experimental dispersion points are consistent

with the calculated dispersion relations. The slight deviation in the TM$_0$ mode should be

attributed to the rough guess of the out-of-plane dielectric constant of PtSe$_2$ ($\varepsilon_\square(\omega) =$

$0.8\varepsilon_\square(\omega)$) to account for its optical anisotropy. An additional dispersion data set for the PtSe$_2$

sample with another thickness, 579 nm, is provided and discussed in Section S9. All in all, these results suggest that the methodology allows to extract the dispersion relations of in-plane propagative EM modes. Also, applying the methodology at different β configurations allows more precise extraction.
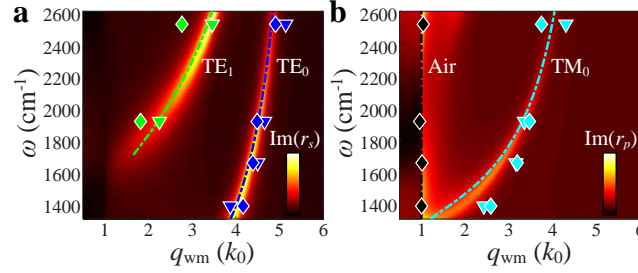
Figure 7. Dispersion analysis. (**a**, **b**) Experimental dispersion data points and theoretical dispersion relations of the TE- and TM-polarized waveguide modes, respectively, for the 696 nm thick PtSe$_2$ sample. The experimental data points (q_{wm}, ω) are obtained by extracting the inverse fringe-periods (q_ρ) from the DFT profiles of the fringe patterns in Figure 6 (Figure S9) and then converting them to the propagation constants (q_{wm}) by numerically solving Equation (1). The extracted points from the $\beta = 64°$ and $\beta = 272°$ profiles are marked by the colored diamonds and inverted triangles, respectively. The theoretical dispersion pseudo-color plot and the dispersion curves are obtained by assuming $\varepsilon_\square(\omega) = 0.8\varepsilon_\square(\omega)$, and then numerical evaluating the imaginary parts of the Fresnel's reflection coefficients (r_s and r_p) and numerically solving the eigenequations (Equation (S17) and (S18)) respectively.

3. Conclusion

In summary, by employing s-SNOM, we performed nano-imaging on PtSe$_2$ flakes. We discovered that the near-field images were sensitive to the orientation of the sample-edges, which suggested that PtSe$_2$ supports dielectric waveguide modes. PtSe$_2$ was found to act optically as a dielectric material in the MIR range with a high refractive index by utilizing both far-field and near-field FTIR spectroscopies. For the near-field FTIR, we studied the near-field response of a material combined with the FP effect, a characteristic effect from a high-refractive-index material. This combinational response has rarely been studied until now. The high-index PtSe$_2$ is a potential material for fabricating MIR waveguides, which are essential for developing integrated photonic circuits in the MIR region,[37] and for developing

high-index dielectric structures for novel applications such as enhancing the performance of MIR PtSe$_2$ photodetectors.[38] We then studied the sample-edge orientation of the characteristic waveguide-mode-induced fringe patterns in the nano-images comprehensively. This study allowed us to precisely determine the momenta of different waveguide-modes in the sample, which, along with the spectroscopic imaging study, further allowed us to extract the dispersion relations of the waveguide-modes. From the dispersion relations, we determined the phase velocities and group velocities of the modes. We found that the waveguide modes in PtSe$_2$ exhibit nearly zero GVD, which allows pulse transmission with very small temporal broadening, which is preferable for telecommunication applications. The technique in this work may be extended to study other EM surface modes supported by other 2D materials or nano-optical-devices. The TE$_0$ mode has the smallest cut-off thickness compared to other modes. Therefore, it is expected that the vdW materials with a small thickness and small imaginary parts of the in-plane and out-of-plane dielectric constants are ideal for fabricating single-mode and low-loss optical waveguides. The single-mode (TE$_0$) exciton polariton (EP) in thin WSe$_2$ waveguides has been studied by s-SNOM in the VIS region using s-polarized light[34] and it is expected to be extended to the MIR region in the future. Besides the tip-launched waveguide modes, which were the main focus in this work, the s-SNOM is also capable of performing nanoscopy of the edge-launched MIR waveguide modes, [39] which possibly possess higher propagation lengths because of the absence of geometrical damping coming from the nature of cylindrical waves.[40] Recently, the edge-launched modes were found to be isolatable from the tip-launched modes by exploiting s-polarized light and performing sample-edge-polarization-dependent nano-imaging.[41] The propagative loss of the modes may also be significantly reduced by performing the experiment in cryogenic conditions[17b] or by replacing the substrate.[34] It is also expected that the near-field technique is able to directly encode the local optical constant of the nanoscale 2D-material waveguides,[42] which favors the theoretical prediction of the dispersion relation

of the modes. Our work paves the way for utilizing high-index TDMCs to develop MIR dielectric nanostructures for nano-optoelectronic and nano-photonic applications.

4. Experimental Methods

Sample fabrication: The substrates used for fabricating the PtSe$_2$ planar waveguides were Silicon wafers with 300 nm thick thermal oxide layers on top. PtSe$_2$ flakes were then transferred onto the substrates by gel-assisted mechanical exfoliation[19] from a high-quality (99.9999% purity) PtSe$_2$ crystal (www.2dsemiconductors.com).

TEM characterization: Cross-sectional TEM and STEM studies were carried out by JEOL JEM-2100F TEM/STEM operated at 200 kV. HAADF STEM Z-contrast images were acquired with an 89 mrad inner angle. The cross-sectional slice of the PtSe$_2$ planar waveguide for the TEM characterization was prepared by the FEI Scios focused ion beam (FIB) microscope.

s-SNOM set-up: The elastic s-SNOM used for nano-optical imaging is the commercial NeaSNOM (www.neaspec.com), which is built based on a tapping-mode AFM. The Pt/Ir-coated silicon-tip (www.nanoworld.com) with a radius of curvature $a \approx 30$ nm oscillates with resonance frequency $\Omega \approx 270$ kHz and with oscillation amplitude $\Delta H \approx 70$ nm. The region between the sample and the oscillating AFM tip is illuminated by a monochromatic MIR laser beam, generating modulated scattering light signals. The MIR laser beam is generated by the quantum cascade laser (QCL) (www.daylightsolutions.com), and the operating wavelength λ_0 was turned from 3.97 to 7.24 μm ($k_0 = 1380 - 2520$ cm^{-1}) in this work. Background scattering signals were eliminated by the use of the pseudo-heterodyne interferometric detection method.[43] Subsequent demodulation of the detected signal by lock-in amplifier at the 3rd order harmonic of the oscillation frequency Ω, thereby generating the pure near-field

(complex) signal σ_3, from whose modulus the s_3 ($= |\sigma_3|$) signals were obtained. The signals are normalized with respect to that of SiO_2. The signal was detected by a mercury cadmium telluride (MCT, HgCdTe) detector which was cooled by liquid nitrogen. The focusing of the laser beam to the AFM tip and the collection of the backscattered light was done by the same parabolic mirror with small collection angle (NA = 0.39). To avoid damage on the AFM tip and the $PtSe_2$ sample when scanning through the edge between the $PtSe_2$ sample and the SiO_2 substrate, the lateral pixel length and the integration time were set to high values: 1024 and 20 ms, respectively. Such a high integration time also allowed reducing the SNR. All the nano-imaging processes were performed at ambient conditions.

Far-field FTIR spectroscopy: The Bruker Vertex 70 with a Hyperion 2000 microscope module was employed for obtaining the reflectance spectra R(ω) (500 – 6000 cm^{-1}) of $PtSe_2$ flakes on Au substrates, with $PtSe_2$ thicknesses 199 nm, 1013 nm, 1708 nm and 2810 nm. The incident MIR beam is randomly polarized and has an incident angle $\theta_{inc} \sim 15°$. Due to the diffraction-limited resolution of this conventional microscope, the $PtSe_2$ sample sizes were prepared to be at least 50 μm × 50 μm. Such large-area samples were prepared by the mechanical exfoliation using thermally sensitive gel films. After transferring the $PtSe_2$ flakes to the Au substrates, the gel films were separated from the flakes by being heated at 90 °C for about 1 min. The phase spectrum was obtained by the KK relation $\theta(\omega) = -\frac{\omega}{\pi}P\int_0^\infty \frac{\ln R(\omega)}{s^2 - \omega^2}ds$,[44] which was performed by using the open-source MATLAB programme.[45] See Section S5 for more details.

Optical constant extraction: For randomly polarized light with small incident angle (~15°), the reflectance spectra of the air/$PtSe_2$/Au three-layer systems were calculated by the equation R = $\frac{\left(r_s^{1\to3}\right)^2 + \left(r_p^{1\to3}\right)^2}{2}$, where $r_s^{1\to3}$ and $r_p^{1\to3}$ are the Fresnel's reflection coefficients of the three-

23

layer system for p- and s- polarized light respectively.[46] These two coefficients were calculated by the use of the transfer-matrix (T-matrix) method, based on the assumed Drude-Lorentz form (Equation (2)) of the optical constant of $PtSe_2$. By turning the parameters to fit the reflectance spectra (Figure S3), the optical constant of $PtSe_2$ was extracted (see Section S4 for more details). The complex refractive index $\tilde{n} = n + i\kappa$ of $PtSe_2$ was obtained from the extracted dielectric constant $\varepsilon = \varepsilon_1 + i\varepsilon_2$ via the relations $n = \frac{1}{\sqrt{2}}\sqrt{\varepsilon_1 + \sqrt{\varepsilon_1^2 + \varepsilon_2^2}}$ and $\kappa = \frac{1}{\sqrt{2}}\sqrt{-\varepsilon_1 + \sqrt{\varepsilon_1^2 + \varepsilon_2^2}}$.

Nano-FTIR spectroscopy: We measured near-field MIR spectra of $PtSe_2$ samples by nano-FTIR which was provided by the commercial NeaSNOM, the one which was employed for IR nano-imaging (s-SNOM), as mentioned above. A MIR broadband laser source, generated by a different-frequency generator (DFG), was utilized for tip-illumination, instead of a monochromatic source for the case of s-SNOM. Same as for s-SNOM, the nano-FTIR employs an asymmetric Michelson interferometer in which one arm is the AFM (where the sample is located), and the other is the reference mirror (RM). In each measurement, by the linear movement of the RM, the backscattered light combined with the reference light and then reached to the MCT detector to generate a near-field interferogram $U(d)$. This interferogram was then demodulated at the 2nd order harmonic of the oscillation frequency of the tip to generate a demodulated interferogram $U_2(d)$. By performing Fourier transform on $U_2(d)$, we obtained the 2nd order demodulated near-field amplitude spectrum $s_2 = |U_2(\omega)|$. To generate near-field spectra covering a large MIR window, different bands of the broadband source were employed so that the spectra extended from about $700 - 2200$ cm^{-1}. The spectra were obtained by averaging the spectra taken at different pixels within an area about 3 μm × 3 μm. For the theoretical calculation, the normalized spectra were calculated by $s_2 = \frac{s_2^{PtSe_2/Au}}{s_2^{Au}} = $

$$\frac{\left(1 + 0.5 r_p^{\text{Air/PtSe}_2/\text{Au}}\right)^2 \alpha_{\text{eff},2}^{\text{PtSe}_2/\text{Au}}}{\left(1 + 0.5 r_p^{\text{Air/Au}}\right)^2 \alpha_{\text{eff},2}^{\text{Au}}}$$, where $\alpha_{\text{eff},2}$ is the 2$^{\text{nd}}$ order Fourier coefficient of the effective

polarizability α_{eff} of the AFM tip. The extended FD model[28] was employed for calculating

$\alpha_{\text{eff},2}^{\text{PtSe}_2/\text{Au}}$ while original FD model was employed for $\alpha_{\text{eff},2}^{\text{Au}}$. See Section S6 for the calculation

steps and chosen parameters.

Dispersion relation calculation: The dispersion pseudo-color maps were obtained by

calculating the loss function $L(q,\omega) = \text{Im}(r)$, where r is the Fresnel's reflection coefficient of

the air/PtSe$_2$/SiO$_2$/Si multi-layer system. Accordingly, the excitation of TE and TM

waveguide modes corresponds to the peaks (bright regions) of the imaginary parts of the

Fresnel's reflection coefficients of the air/PtSe$_2$/SiO$_2$/Si 4-layer system for *p*- and *s*-polarized

light, respectively. For the dispersion curves, they were obtained by numerically, but not

analytically, solving the transcendental eigenequations of the waveguide modes, obtained by

finding the condition of the pole of the r (Equation (S17) and (S18)). All the calculations were

based on the use of the in-plane complex dielectric constant $\varepsilon_\square$ of PtSe$_2$ obtained from the

FTIR measurements. In order to fit the experimental dispersion data points of the TM modes,

the out-of-plane dielectric constant $\varepsilon_\square$ was assumed to be 0.8 times the in-plane value. See

Section S7 for the further detail of the dispersion calculation.

Supporting Information
Supporting Information is available from the Wiley Online Library or from the author.

References

[1]   a) A. I. Kuznetsov, A. E. Miroshnichenko, M. L. Brongersma, Y. S. Kivshar, B. Luk'yanchuk, *Science* **2016**, 354, aag2472; b) G. Kang, J. Yoo, J. Ahn, K. Kim, *Nano Today* **2015**, 10, 22.

[2]   L. Cao, J. S. White, J.-S. Park, J. A. Schuller, B. M. Clemens, M. L. Brongersma, *Nat. Mater.* **2009**, 8, 643.

[3]   G. Grzela, R. Paniagua-Domínguez, T. Barten, Y. Fontana, J. A. Sánchez-Gil, J. Gómez Rivas, *Nano Lett.* **2012**, 12, 5481.

[4]   S. J. Kim, I. Thomann, J. Park, J.-H. Kang, A. P. Vasudev, M. L. Brongersma, *Nano Lett.* **2014**, 14, 1446.

[5]   M. L. Brongersma, Y. Cui, S. Fan, *Nat. Mater.* **2014**, 13, 451.

[6]   M. R. Shcherbakov, D. N. Neshev, B. Hopkins, A. S. Shorokhov, I. Staude, E. V. Melik-Gaykazyan, M. Decker, A. A. Ezhov, A. E. Miroshnichenko, I. Brener, A. A. Fedyanin, Y. S. Kivshar, *Nano Lett.* **2014**, 14, 6488.

[7]   a) S. Jahani, Z. Jacob, *Nat. Nanotechnol.* **2016**, 11, 23; b) S. R. Amanaganti, M. Ravnik, J. Dontabhaktuni, *Sci. Rep.* **2020**, 10, 15599.

[8]   a) K. F. Mak, J. Shan, *Nat. Photonics* **2016**, 10, 216; b) F. Xia, H. Wang, D. Xiao, M. Dubey, A. Ramasubramaniam, *Nat. Photonics* **2014**, 8, 899.

[9]   M. N. Gjerding, R. Petersen, T. G. Pedersen, N. A. Mortensen, K. S. Thygesen, *Nat. Commun.* **2017**, 8, 320.

[10]   a) R. Verre, D. G. Baranov, B. Munkhbat, J. Cuadra, M. Käll, T. Shegai, *Nat. Nanotechnol.* **2019**, 14, 679; b) T. D. Green, D. G. Baranov, B. Munkhbat, R. Verre, T. Shegai, M. Käll, *Optica* **2020**, 7, 680.

[11]   a) Z. Fei, M. Scott, D. Gosztola, J. Foley IV, J. Yan, D. Mandrus, H. Wen, P. Zhou, D. Zhang, Y. Sun, *Phys. Rev. B* **2016**, 94, 081402; b) D. Hu, K. Chen, X. Chen, X. Guo, M. Liu, Q. Dai, *Adv. Mater.* **2019**, 1807788.

[12]   G. Guo, W. Liang, *J. Phys. C: Solid State Phys.* **1986**, 19, 995.

[13]   a) H. Huang, S. Zhou, W. Duan, *Phys. Rev. B* **2016**, 94, 121117; b) K. Zhang, M. Yan, H. Zhang, H. Huang, M. Arita, Z. Sun, W. Duan, Y. Wu, S. Zhou, *Phys. Rev. B* **2017**, 96, 125102; c) M. Yan, H. Huang, K. Zhang, E. Wang, W. Yao, K. Deng, G. Wan, H. Zhang, M. Arita, H. Yang, Z. Sun, H. Yao, Y. Wu, S. Fan, W. Duan, S. Zhou, *Nat. Commun.* **2017**, 8, 257.

[14]   J. Duan, Y. Li, Y. Zhou, Y. Cheng, J. Chen, *Adv. Phys.: X* **2019**, 4, 1593051.

[15]   X. Hu, K. P. Wong, L. Zeng, X. Guo, T. Liu, L. Zhang, Q. Chen, X. Zhang, Y. Zhu, K. H. Fung, S. P. Lau, *ACS Nano* **2020**, 14, 6276.

[16]   G. Wang, Z. Wang, N. McEvoy, P. Fan, W. J. Blau, *Adv. Mater.* **2020**, n/a, 2004070.

[17]   a) D. Hu, X. Yang, C. Li, R. Liu, Z. Yao, H. Hu, S. N. G. Corder, J. Chen, Z. Sun, M. Liu, *Nat. Commun.* **2017**, 8, 1471; b) F. Hu, Y. Luan, M. Scott, J. Yan, D. Mandrus, X. Xu, Z. Fei, *Nat. Photonics* **2017**, 11, 356.

[18]   H. Li, *J. Phys. Chem. Ref. Data* **1980**, 9, 561.

[19]   a) P. Budania, P. T. Baine, J. H. Montgomery, D. W. McNeill, S. N. Mitchell, M. Modreanu, P. K. Hurley, *Micro Nano Lett.* **2017**, 12, 970; b) A. Castellanos-Gomez, M. Buscema, R. Molenaar, V. Singh, L. Janssen, H. S. Van Der Zant, G. A. Steele, *2D Mater.* **2014**, 1, 011002.

[20]   Z. Fei, G. O. Andreev, W. Bao, L. M. Zhang, A. S. McLeod, C. Wang, M. K. Stewart, Z. Zhao, G. Dominguez, M. Thiemens, *Nano Lett.* **2011**, 11, 4701.

[21]   A. D. Rakić, A. B. Djurišić, J. M. Elazar, M. L. Majewski, *Appl. Opt.* **1998**, 37, 5271.

[22]   O. J. Clark, F. Mazzola, J. Feng, V. Sunko, I. Marković, L. Bawden, T. K. Kim, P. King, M. S. Bahramy, *Phys. Rev. B* **2019**, 99, 045438.

[23]   H. Yang, M. Schmidt, V. Süss, M. Chan, F. F. Balakirev, R. D. McDonald, S. S.
       Parkin, C. Felser, B. Yan, P. J. Moll, *New J. Phys.* **2018**, 20, 043008.
[24]   H. W. Verleur, *J. Opt. Soc. Am.* **1968**, 58, 1356.
[25]   M. K. Gunde, *Phys. B* **2000**, 292, 286.
[26]   A. Beal, H. Hughes, *J. Phys. C: Solid State Phys.* **1979**, 12, 881.
[27]   A. Cvitkovic, N. Ocelic, R. Hillenbrand, *Opt. Express* **2007**, 15, 8550.
[28]   B. Hauer, A. P. Engelhardt, T. Taubner, *Opt. Express* **2012**, 20, 13173.
[29]   K. Zeppenfeld, *Opt. Commun.* **1970**, 1, 377.
[30]   A. Beal, W. Liang, H. Hughes, *J. Phys. C: Solid State Phys.* **1976**, 9, 2449.
[31]   S. C. Bayliss, W. Y. Liang, *J. Phys. C: Solid State Phys.* **1985**, 18, 3327.
[32]   Y. Bertrand, G. Leveque, C. Raisin, F. Levy, *J. Phys. C: Solid State Phys.* **1979**, 12,
       2907.
[33]   F. Walla, M. M. Wiecha, N. Mecklenbeck, S. Beldi, F. Keilmann, M. D. Thomson, H.
       G. Roskos, *Nanophotonics* **2018**, 7, 269.
[34]   F. Hu, Y. Luan, J. Speltz, D. Zhong, C. Liu, J. Yan, D. Mandrus, X. Xu, Z. Fei, *Phys.
       Rev. B* **2019**, 100, 121301.
[35]   B.-Y. Jiang, L. Zhang, A. Castro Neto, D. Basov, M. Fogler, *J Appl Phys* **2016**, 119,
       054305.
[36]   P. A. D. Gonçalves, N. M. Peres, *An introduction to graphene plasmonics*, World
       Scientific, Hackensack, NJ **2016**.
[37]   Y. Zou, S. Chakravarty, C.-J. Chung, X. Xu, R. T. Chen, *Photonics Res.* **2018**, 6, 254.
[38]   X. Yu, P. Yu, D. Wu, B. Singh, Q. Zeng, H. Lin, W. Zhou, J. Lin, K. Suenaga, Z. Liu,
       Nat. Commun. **2018**, 9, 1545.
[39]   M. Xue, Q. Zheng, R. Chen, L. Bao, S. Du, J. Chen, *Nanoscale* **2019**, 11, 14113.
[40]   S. Dai, Q. Ma, Y. Yang, J. Rosenfeld, M. D. Goldflam, A. McLeod, Z. Sun, T. I.
       Andersen, Z. Fei, M. Liu, Y. Shao, K. Watanabe, T. Taniguchi, M. Thiemens, F.
       Keilmann, P. Jarillo-Herrero, M. M. Fogler, D. N. Basov, *Nano Lett.* **2017**, 17, 5285.
[41]   L. Wang, R. Chen, M. Xue, S. Liu, J. H. Edgar, J. Chen, *Nanoscale* **2020**, 12, 8188.
[42]   a) A. A. Govyadinov, S. Mastel, F. Golmar, A. Chuvilin, P. S. Carney, R. Hillenbrand,
       ACS Nano **2014**, 8, 6911; b) A. S. McLeod, P. Kelly, M. Goldflam, Z. Gainsforth, A.
       J. Westphal, G. Dominguez, M. H. Thiemens, M. M. Fogler, D. Basov, *Phys. Rev. B*
       2014, 90, 085136.
[43]   N. Ocelic, A. Huber, R. Hillenbrand, *Appl. Phys. Lett.* **2006**, 89, 101124.
[44]   F. C. Jahoda, *Phys. Rev.* **1957**, 107, 1261.
[45]   V. Lucarini, J. J. Saarinen, K. E. Peiponen, E. M. Vartiainen, *Kramers-Kronig
       Relations in Optical Materials Research*, Springer-Verlag, Berlin, Heidelberg **2005**.
[46]   M. Born, E. Wolf, *Principles of Optics*, Cambridge University Press, Cambridge, U.K.
       1999.